Compression-based nonnegative tensor CP decomposition of hyperspectral big data

Miguel Angel Veganzones, Jérémy E Cohen, Rodrigo Cabral Farias, Jocelyn Chanussot, Pierre Comon

Compression-based nonnegative tensor CP decomposition of hyperspectral big data

Miguel A. Veganzones, *Member, IEEE,* Jeremy E. Cohen, Rodrigo Cabral Farias, Jocelyn Chanussot, *Fellow, IEEE*, and Pierre Comon, *Fellow, IEEE*.

Abstract

New hyperspectral missions will collect huge amounts of hyperspectral data. Besides, it is possible now to acquire time series and multiangular hyperspectral images. The process and analysis of these big data collections will require common hyperspectral techniques to be adapted or reformulated. The tensor decomposition, *a.k.a.* multiway analysis, is a technique to decompose multiway arrays, that is, hypermatrices with more than two dimensions (ways). Hyperspectral time series and multiangular acquisitions can be represented as a 3-way tensor. Here, we apply Canonical Polyadic tensor decomposition techniques to the blind analysis of hyperspectral big data. In order to do so, we use a novel compression-based nonnegative CP decomposition. We show that the proposed methodology can be interpreted as multilinear blind spectral unmixing, a higher order extension of the widely known spectral unmixing. In the proposed approach, the big hyperspectral tensor is decomposed in three sets of factors corresponding to spectral signatures, their spatial distribution and temporal/angular changes. We provide experimental validation using a study case of the snow coverage of the French Alps during the snow season.

Index Terms

Big data, hyperspectral, nonnegative tensor decomposition, CP decomposition, compression, time series.

I. Introduction

Imaging spectroscopy [1] (a.k.a. hyperspectral imaging) is concerned with the measurement, analysis, and interpretation of spectra acquired from a given scene or object [2]. The impact of hyperspectral imaging in remote sensing during the last two decades has been huge [2]–[4]. The interest of the remote sensing community in the subject has grown up to be comparable to that of radar technology, with a clear increasing trend in the former and a stabilization or decrease in the latter [5]. The International Spaceborne Imaging Spectroscopy Technical Committee (ISIS TC) of IEEE GRSS has recently informed of an increasing number of terrestrial space-based civilian imaging spectroscopy missions currently in preparation or in the planning phase [6]. In addition to the

The authors are with GIPSA-Lab, 11 rue des Mathematiques, Grenoble Campus, BP.46, F-38402 St Martin d'Heres cedex, France. e-mail: {miguel-angel.veganzones, jeremy.cohen, rodrigo.cabral-farias, jocelyn.chanussot, pierre.comon}@gipsa-lab.fr

This work has received funding from the European Research Council under the European Communitys Seventh Framework Programme FP7/2007-2013 Grant Agreement no. 320594, "DECODA".

Earth Observation (EO) missions, remote sensing hyperspectral imaging has been used for planetological studies [7] and deep space exploration [8]. Also, it has proved useful for industrial and laboratory applications, using small commercial instruments.

Hyperspectral images (HSI) are usually stored in a nonnegative matrix form, $\boldsymbol{X} \in \mathbb{R}_{+}^{N \times D}$, where N denotes the number of pixels in the image and D denotes the number of spectral bands. For most of the modern hyperspectral sensors, the number of acquired spectral bands is in the order of hundreds, $O(D) \approx 10^2$, *e.g.*, EnMAP[1], PRISMA[2] or HYPERION[3] sensors capture between 220 and 238 spectral bands covering the spectrum in a range of wavelengths between 0.4μm and 2.5μm. However, it is expected that future sensors will collect thousands of bands, *e.g.*, IASI sensor[4] captures 8461 spectral bands in wavelengths covering the range $3.62 - 15.5\mu$m. The number of pixels composing a HSI are usually in the order of hundreds of thousands, $O(N) \approx 10^6$. The high spatial and spectral dimensionality of the HSI makes their analysis very computationally costly. Furthermore, new missions and sensor developments are making it possible to collect time series of hyperspectral data, *e.g.* MODIS mission[5], and multiangular images, *e.g.* CRISM mission[6]. The huge amount of hyperspectral data that will be delivered in the near future encouraged us to consider hyperspectral image analysis from a big data point of view. These hyperspectral big data will pose new challenges to hyperspectral image analysis. For instance, new techniques to extract the low-rank relevant information will be necessary.

Here, we propose to make use of techniques from tensor analysis [9] (a.k.a. multiway or multiarray analysis) to face this challenge. Time series or multiangle hyperspectral big data could be understood as nonnegative tensors, $\boldsymbol{\mathcal{X}} \in \mathbb{R}_{+}^{N \times D \times T}$, where N, D and T denote the dimensionality of the spatial, spectral and time/angle ways, respectively. One of the most successful techniques to decompose tensors in low-rank terms is the Canonical Polyadic decomposition (CP) [10], sometimes coined Candecomp/Parafac [11]. The CP decomposition could be understood as an extension of the linear unmixing of 2-way (spatial and spectral) hyperspectral data [12] to the multilinear unmixing of multiway (more than two) hyperspectral tensors. Conventional spectral unmixing aims to decompose an hyperspectral image into the spectral signatures of the materials present in the image and their spatial distributions, known respectively as *endmembers* and *fractional abundances*. Hence, we introduce in Section II the CP decomposition as a technique for blind spectral unmixing of hyperspectral big data. Rank-one factors are expected to be related to spatial abundances, spectral signatures and changes in time/angle. The proposed methodology is blind in the sense that no *a priori* information is needed, for example, when the spectral signatures of the materials in the image are unknown.

Often, conventional spectral unmixing techniques make use of a set of spectral signatures of materials taken on

[1]http://www.enmap.org/

[2]http://www.asi.it/en/activity/earth_observation/prisma_

[3]http://eo1.usgs.gov/sensors/hyperion

[4]http://wdc.dlr.de/sensors/iasi/

[5]http://modis.gsfc.nasa.gov/

[6]http://crism.jhuapl.edu/

the field or in lab, and collected in a spectral library [13]. Otherwise, the endmembers are estimated from the data using geometrical or statistical spectral unmixing algorithms [12]. Then, the estimation of the spatial fractional abundances is modeled as an optimization problem usually solved by a constrained least squares algorithm. Some recent methods have proposed to jointly estimate the endmembers and their fractional abundances [14], [15]. The proposed methodology allows to jointly unmix big data hyperspectral time series or multiangle acquisitions, decomposing the data into a set of spectral, spatial and time factors, that eventually play the role of endmembers, fractional abundances and time/angle changes.

An important aspect of HSIs is that they relate to physical quantities of the objects composing the scene, *e.g.*, the radiance or the reflectance, which are real nonnegative. In addition, the modeling assumed involves spectral, abundance, or scaling quantities, which are also nonnegative. Hence, it is desirable to impose all terms in the CP decomposition described in Section II to be nonnegative. Moreover, there are some practical issues that should be addressed when computing the nonnegative CP decomposition of hyperspectral tensors. In fact, the big data nature of hyperspectral tensors makes the computational cost of nonnegative CP decomposition algorithms prohibitive for real applications. Thus, it is necessary to develop special-purpose algorithms able to reduce memory requirements and to speed up computations, while enforcing nonnegativity of the CP decomposition. Recently, a solution to this issue has been proposed in [16], as well as two compression-based nonnegative CP decomposition algorithms. This issue is addressed in the paper.

A. Contribution

We propose the use of compression-based nonnegative CP decomposition algorithms to analyze big hyperspectral data tensors, *i.e.* hyperspectral time series or hyperspectral multiangle acquisitions. The proposed methodology could be interpreted as an extension of the linear spectral unmixing to higher orders, that is, a multilinear spectral unmixing. We provide quantitative and qualitative evidence of the validity of the proposed methodology, using a dataset obtained by the MODIS hyperspectral sensor during the 2012 snow season in the French Alps.

The remainder of the paper is organized as follows. In Sec. II we overview the topic of tensor decompositions, *a.k.a.* multiway analysis. In Sec. III we propose an adaptation of the CP decomposition to hyperspectral big data. In Sec. IV we provide experimental evaluation of the proposed methodology using a study case of a hyperspectral time series of MODIS acquisitions. Finally, we give some conclusions in Sec. V.

II. Tensor decomposition / Multiway analysis

A. Rank revealing decomposition

For our need, a third order tensor $\boldsymbol{\mathcal{X}}$ of size $N \times D \times T$ will be merely assimilated to its representation by a three-way array $\mathcal{X}_{ijk}$, $1 \leq i \leq N$, $1 \leq j \leq D$, $1 \leq k \leq T$. Note that tensors of order two are then just matrices. Among the set of tensors, the class of so-called *decomposable* tensors play a central role. These tensors, also sometimes called *pure* or *elementary*, may be seen as a discretization of functions whose variable separate:

$$\mathcal{D}_{ijk} = a_i b_j c_k.$$

It is worth noting that there are obviously infinitely many ways to write a decomposable tensor as a product of single-index components, because of scaling indeterminacies. In fact, one can replace $a_i b_j c_k$ by $(a_i/\alpha)(b_j/\beta)(\alpha\beta c_k)$ for any pair of nonzero scalars (α, β). Any finite tensor can be written as a finite sum of decomposable tensors:

$$\boldsymbol{\mathcal{X}} = \sum_{r=1}^{R} \lambda_r \boldsymbol{\mathcal{D}}(r), \tag{1}$$

where λ_r are real strictly positive. The *rank* of tensor $\boldsymbol{\mathcal{X}}$ is defined as the minimal number R of terms necessary for the equality above to hold exactly. In that case, expression (1) is called the *Canonical Polyadic* (CP) decomposition of $\boldsymbol{\mathcal{X}}$. Decomposable tensors have then, by definition, a rank equal to 1. This definition of rank is consistent with the usual definition of matrix rank, when tensors of order two are considered. In practice, it may be useful to impose tensors $\boldsymbol{\mathcal{D}}(r)$ to be of unit norm. With this normalization, λ_r can be compared to singular values in the case of tensors of order two.

A first consequence of the nonnegativity constraint is that it has an impact on the value of the tensor's rank. In fact, the (matrix or tensor) rank computed in $\mathbb{R}^+$ may be strictly larger than the rank computed in $\mathbb{R}$ [17], [18]. For this reason, when all quantities involved in the CP decomposition are real nonnegative, the minimal value of R is called the *nonnegative rank*.

B. Factor matrices

Another writing of the CP decomposition makes it more explicit that the data tensor $\boldsymbol{\mathcal{X}}$ is related to a diagonal tensor $\boldsymbol{\mathcal{L}}$ via a multilinear transform. To see this, denote $\mathcal{D}_{ijk}(r) = A_{ir}B_{jr}C_{kr}$, where factor matrices $\boldsymbol{A}$, $\boldsymbol{B}$ and $\boldsymbol{C}$ are of size $N \times R$, $D \times R$ and $T \times R$, respectively. Then, it is easy to show that (1) can be rewritten as:

$$\mathcal{X}_{ijk} = \sum_{r=1}^{R} A_{ir}B_{jr}C_{kr}\lambda_r. \tag{2}$$

Now define $\boldsymbol{\mathcal{L}}$ as the diagonal tensor of size $R \times R \times R$ containing the R scaling factors λ_r. Then, we agree to denote compactly the polyadic decomposition (2) as

$$\boldsymbol{\mathcal{X}} = (\boldsymbol{A}, \boldsymbol{B}, \boldsymbol{C}) \cdot \boldsymbol{\mathcal{L}}. \tag{3}$$

The major difference between (1) and (2-3) is that the latter made use of one writing of $\boldsymbol{\mathcal{D}}(r)$ among others, and hence cannot pretend to be unique because of this arbitrary choice. On the other hand, this writing is unavoidable when implementing numerical algorithms, hence its importance. This issue will be addressed in Subsection II-D.

C. Approximation

In practice, the data tensor is subject to modeling errors or measurement noise, and it is convenient to find its best rank-R approximation by minimizing the following objective function

$$\Upsilon(\boldsymbol{A}, \boldsymbol{B}, \boldsymbol{C}, \boldsymbol{\mathcal{L}}) = \|\boldsymbol{\mathcal{X}} - (\boldsymbol{A}, \boldsymbol{B}, \boldsymbol{C}) \cdot \boldsymbol{\mathcal{L}}\|, \tag{4}$$

for some well chosen norm, instead of attempting to compute the exact CP decomposition (2). It is now known that tensors of order 3 or larger do not always admit a rank-R approximate, when $R > 1$, especially in $\mathbb{R}$ or $\mathbb{C}$.

But fortunately, it has been shown in [18] that this obstacle does no longer holds for nonnegative tensors, and that the problem is well-posed in $\mathbb{R}^+$: best lower nonnegative rank approximates always exist.

D. Uniqueness

The exact CP decomposition (1) is unique if the rank R is not too large. In fact, several sufficient upper bounds have been proposed in the literature [19], [20]. In particular, from [20] we know that almost every 3rd order tensor of rank smaller than the bound R_o below has a unique CP decomposition:

$$R_o = \left\lceil \frac{NDT}{N + D + T - 2} \right\rceil . \tag{5}$$

However, uniqueness results available in the literature apply only to the exact CP decomposition, and not to an approximation like (4), which must unavoidably be computed in practice. Therefore, we shall also rely on a recent result of [21], which states that almost every nonnegative tensor of nonnegative rank larger than R admits a unique best approximate of nonnegative rank R, which in turn has a unique CP decomposition if condition $R < R_o$ holds true.

III. Hyperspectral big data CP decomposition

A. Extending the linear unmixing model

The linear unmixing model is the simplest and most widely used model for recovering spectra and abundances of a scenery from an hyperspectral image. By imposing some constraints on the factors, the bilinear decomposition becomes unique, and the recovered factors bear physical meaning as actual spectra and abundances. In fact, the linear unmixing model is a particular case of CP decomposition where the data tensor $\boldsymbol{\mathcal{X}}$ is a matrix, i.e. $T = 1$, and additional constraints are added. Thus in the presence of a third variability source, say time or angle, it is natural to study the constrained CP decomposition of multiway hyperspectral data.

However, unlike its bilinear counterpart, the multiway model cannot be *a priori* deduced from a physical reasoning. Indeed, a multiplicative model will not explain the sophisticated temporal or angular evolution of different materials which includes appearance/disappearance and strong non-linearities. For this reason, applying the CP decomposition to $\boldsymbol{\mathcal{X}}$ should rather be understood as decomposing the data on rank-one meaningful linear subspaces maximizing the explained variance, very much like a non-orthogonal PCA. Yet, knowing the bilinear model bears physical interpretability. We hope the recovered factors $\boldsymbol{A}$, $\boldsymbol{B}$ and $\boldsymbol{C}$ can be interpreted respectively as spatial, spectral and time/angle ways of R materials. Moreover, the same material might be decomposed in two or more rank-one factors to capture its complex variability. Also, nonnegativity constraints should be imposed on all three factor matrices to ensure both algorithmic convergence and physical interpretability.

B. Nonnegative CP approximation

It is well known in the optimization community that computing the nonnegative CP decomposition of a positive tensor is a difficult problem. Given a multiway data set $\boldsymbol{\mathcal{X}}$, we want to solve the following minimization problem:

$$\begin{aligned} &\text{argmin } \|\boldsymbol{\mathcal{X}} - (\boldsymbol{A}, \boldsymbol{B}, \boldsymbol{C}) \cdot \boldsymbol{\mathcal{L}}\|_F^2 \\ &\text{w.r.t. } \boldsymbol{A}, \boldsymbol{B}, \boldsymbol{C} \\ &\text{s.t. } \boldsymbol{A} \succeq 0, \boldsymbol{B} \succeq 0, \boldsymbol{C} \succeq 0, \end{aligned} \tag{6}$$

where $\|\cdot\|_F$ denotes the Frobenius norm. This problem is highly non-convex, yet many algorithms provide rather precise but costly computation, and these algorithms can be divided into two main classes:

- *All-at-once gradient-based descent, e.g.* [22]: all CP parameters are updated at the same time using a gradient scheme (standard or conjugate gradient) and nonnegativity constraints are implemented through barriers or soft penalizations.
- *Alternating minimization*: the cost function is minimized in an alternating way for each factor ($\boldsymbol{A}$, $\boldsymbol{B}$ or $\boldsymbol{C}$) while the others are fixed. The most commonly used method for nonnegative CP decomposition is alternating nonnegative least squares (ANLS), *e.g.* [23].

C. Handling big data through compression

Now in hyperspectral imaging, as stated in the introduction, the usual dimensions of the data tensor are huge. In this setting, the workhorse techniques described briefly above can fail to handle all the data within the memory of the computer, or can converge very slowly.

Large tensors decomposition is actually a hot topic in the tensor decomposition area, especially when constraints are included in the optimization problem. An approach to handle large tensor decomposition is through the use of compression. The general idea is that the original data array $\boldsymbol{\mathcal{X}}$ can be equivalently represented by one or a few arrays $\boldsymbol{\mathcal{X}}_c$ with reduced dimensions $N_c \times D_c \times T_c$. The compressed tensor is then decomposed by solving

$$\begin{aligned} &\text{argmin } \Upsilon = \|\boldsymbol{\mathcal{X}}_c - (\boldsymbol{A}_c, \boldsymbol{B}_c, \boldsymbol{C}_c)\|_F^2 \\ &\text{w.r.t. } \boldsymbol{A}_c, \boldsymbol{B}_c, \boldsymbol{C}_c, \end{aligned} \tag{7}$$

where $\boldsymbol{A}_c$, $\boldsymbol{B}_c$, $\boldsymbol{C}_c$ are compressed versions of the original factor matrices, with reduced number of rows N_c, D_c, T_c, but the same number of columns R. For simplification purposes the diagonal matrix of scalings is absorbed in $\boldsymbol{C}_c$. Note that, after the compressed factors are obtained, a decompression operation is carried out to recover the factors in the original dimensions.

In the literature, two main approaches have been proposed to compress the tensor array. The first proposed approach [24, p. 92] is through an approximation of the High Order Singular Value Decomposition (HOSVD). The HOSVD [25] approximates the original data in the following way

$$\boldsymbol{\mathcal{X}}_{ijk} \approx \sum_{lmn}^{N_c, D_c, T_c} \boldsymbol{U}_{il} \boldsymbol{V}_{jm} \boldsymbol{W}_{kn} \left[\boldsymbol{\mathcal{X}}_c\right]_{ijk}, \tag{8}$$

or using the same notation as in the CP model

$$\boldsymbol{\mathcal{X}} \approx (\boldsymbol{U}, \boldsymbol{V}, \boldsymbol{W})\, \boldsymbol{\mathcal{X}}_c, \tag{9}$$

where $\boldsymbol{U}$, $\boldsymbol{V}$ and $\boldsymbol{W}$ are matrices with orthogonal unit-norm columns. In practice, these matrices are obtained by truncating the first N_c, D_c and T_c left singular vectors of the 3 unfoldings of $\boldsymbol{\mathcal{X}}$ (unfoldings are different concatenations of matrix slices of the tensor, see *e.g* [9] and references therein). Note that, in this case, the compressed and uncompressed factors are related in the following way:

$$\boldsymbol{A} \approx \boldsymbol{U}\boldsymbol{A}_c, \quad \boldsymbol{B} \approx \boldsymbol{V}\boldsymbol{B}_c, \quad \boldsymbol{C} \approx \boldsymbol{W}\boldsymbol{C}_c, \tag{10}$$

which shows that $\boldsymbol{U}$, $\boldsymbol{V}$ and $\boldsymbol{W}$ can be seen as decompression operators.

The second approach, called PARACOMP [26], consists in generating multiple compressed tensors through multiple U^i, V^i and W^i, but in this case, these matrices are neither deterministic, neither data dependent. The vectors forming the columns of these matrices are independently drawn from an independent and identically distributed multivariate Gaussian distribution. Since there are multiple compressed factors $\boldsymbol{A}_c^i$, the uncompressed factors are obtained by merging the results. After correcting the permutations between different $\boldsymbol{A}_c^i$, the results are merged through the solution of a linear system of equations. For example, factor A is obtained by solving

$$\left[U^1 \ \cdots \ U^I\right]^\top \boldsymbol{A} = \begin{bmatrix} \boldsymbol{A}_c^1 \\ \vdots \\ \boldsymbol{A}_c^I \end{bmatrix}. \tag{11}$$

D. Algorithms for large hyperspectral data

Both approaches presented above may decrease substantially the complexity required for the unconstrained CP decomposition, thus solving the big data issue, which is fundamental to the extension of the linear mixing model to a multilinear one. Still an important issue persists, *how to deal with nonnegativity constraints?* The approaches presented above cannot directly handle nonnegative constraints, since nonnegativity cannot be imposed directly in the compressed space. Therefore, specialized algorithms are needed to deal with nonnegativity in these two approaches.

In the HOSVD approach, we need to solve (7) under the following constraints

$$\boldsymbol{U}\boldsymbol{A}_c \succeq 0, \quad \boldsymbol{V}\boldsymbol{B}_c \succeq 0, \quad \boldsymbol{W}\boldsymbol{C}_c \succeq 0. \tag{12}$$

To solve this problem, adapted instances of the two main classes of algorithms for nonnegative CP decomposition are proposed in [16]. In the all-at-once gradient descent setting, the Compressed Conjugate Gradient (CCG) algorithm is proposed, while a modification of ANLS, Projected and Compressed ALS (ProCo ALS), is presented in the alternating setting. A solution similar to ProCo ALS is also proposed in [27].

In the PARACOMP approach, an ADMM projection algorithm is proposed to add nonnegativity constraints [28]. But it has been noted in [27] that this approach is very sensitive to noise, which is a huge drawback for hyperspectral

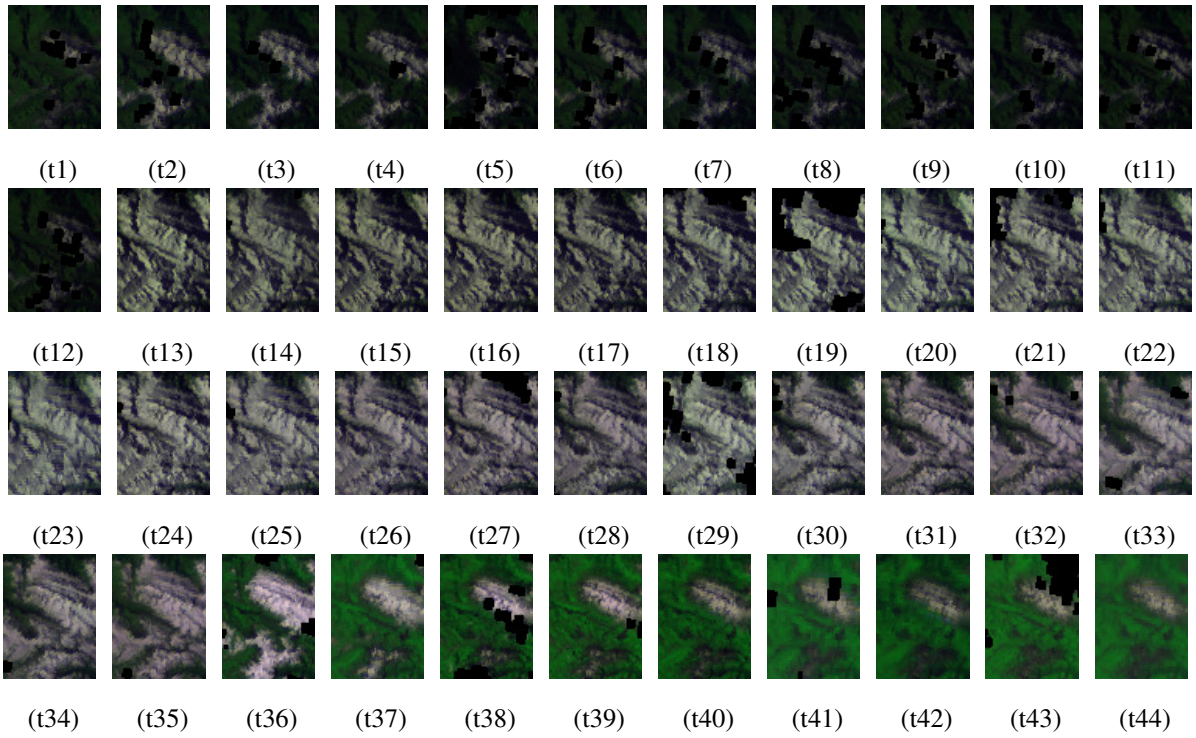

Fig. 1. False color images of the 44 time acquisitions (cloud pixels are depicted in black).

applications. Therefore, in what follows we will briefly explain and apply only the HOSVD based algorithms: CCG and ProCo ALS.

1) CCG: to include the nonnegative constraints in the minimization of $\Upsilon\left(\boldsymbol{A}_c, \boldsymbol{B}_c, \boldsymbol{C}_c\right)$ soft penalization terms $f\left(\left[\boldsymbol{U}\boldsymbol{A}_c\right]_{ij}\right)$ are added in order to increase the objective function whenever $\left[\boldsymbol{U}\boldsymbol{A}_c\right]_{ij}$ are negative. Stacking all elements of the factor matrices in a single vector $\boldsymbol{\theta} = \mathbf{vec}\left(\boldsymbol{A}_c^\top, \boldsymbol{B}_c^\top, \boldsymbol{C}_c^\top\right)$, the modified objective function becomes

$$\Upsilon_p = \Upsilon\left(\boldsymbol{\theta}\right) + \frac{1}{R\left(N+D+T\right)}\left[\sum_{i,j}^{N,R} f\left(\left[\boldsymbol{U}\boldsymbol{A}_c\right]_{ij}\right) + \cdots\right],$$

where f is a sigmoidal function, for example an hyperbolic tangent function. Then, applying the conjugate gradient method [29, p. 101] to this function gives the CCG method. At iterate $k+1$, the CCG update $\hat{\boldsymbol{\theta}}^{k+1}$ is given by

$$\hat{\boldsymbol{\theta}}^{k+1} = \hat{\boldsymbol{\theta}}^{k} + \mu_k \mathbf{s}^k, \tag{13}$$

where μ_k is the step size given by backtracking line search [29, p. 37] and $\mathbf{s}^k$ is the conjugate gradient direction, for example using the Polak-Ribière method [29, p. 122], this direction is given by

$$\mathbf{s}^{k+1} = \mathbf{p}^{k+1} + \frac{\left(\mathbf{p}^{k+1}\right)^\top\left(\mathbf{p}^{k+1} - \mathbf{p}^{k}\right)}{\left\|\mathbf{p}^k\right\|^2}\mathbf{s}^k, \tag{14}$$

where $\mathbf{p}^k$ denotes the negative gradient of Υ_p at the point $\hat{\boldsymbol{\theta}}^{k}$.

2) ALS: in the alternating setting, to update each factor we need to solve a least squares problem with linear inequality constraints. The idea of ProCo ALS is to carry out an approximate projection of the unconstrained least squares (LS) solution on the set of feasible solutions. This approximate projection is given in three steps: first the factor is decompressed (D), then the decompressed factor is projected onto the nonnegative orthant (P), and, finally, the result of the projection is recompressed (R). The four steps of each ProCo ALS iteration to update the factor $\boldsymbol{A}_c$, denoted here $\hat{\mathbf{A}}_{pc}^{k+1}$, are detailed below:

$$\begin{aligned} &\text{LS:} && \hat{\mathbf{A}}_c^{k+1} = \boldsymbol{X}_c^{(1)} \left(\hat{\mathbf{C}}_{pc}^{k} \odot \hat{\mathbf{B}}_{pc}^{k} \right)^{\dagger} \\ &\text{Approx. proj.} && \begin{cases} \text{D:} & \hat{\mathbf{A}}^{k+1} = \boldsymbol{U} \hat{\mathbf{A}}_c^{k+1} \\ \text{P:} & \left[\hat{\mathbf{A}}^{k+1} \right]_+ := \max \left(\mathbf{0}, \hat{\mathbf{A}}^{k+1} \right) \\ \text{R:} & \hat{\mathbf{A}}_{pc}^{k+1} = \boldsymbol{U}^{\top} \left[\hat{\mathbf{A}}^{k+1} \right]_+ \end{cases} \end{aligned} \tag{15}$$

where $\odot$ denotes the Khatri-Rao product, $\dagger$ indicates the pseudoinverse, $\boldsymbol{X}_c^{(1)}$ is the unfolding in the first way of $\boldsymbol{\mathcal{X}}_c$ and $\max(\cdot,\cdot)$ denotes the element wise maximum. To obtain the updates $\hat{\mathbf{B}}_{pc}^{k+1}$ and $\hat{\mathbf{C}}_{pc}^{k+1}$, the same procedure is applied with the appropriate unfolding of $\boldsymbol{\mathcal{X}}_c$ and decompression operators.

IV. Study case: hyperspectral time series

A. Dataset

The dataset is a subset of a longitudinal daily acquisition of MODIS hyperspectral sensor for the same scene in the Alps (France) during the 2012 snow season. The data has been pre-processed to improve the spatial resolution to 250m. From the original dataset we have selected 44 acquisitions with a cloud presence lower than 30%. Each image is of 80×60 pixels size with seven spectral bands measuring the radiance at the sensor.

Fig. III-C shows a false color image of the 44 acquisitions. It can be appreciated that some permanent snow/ice lies on the top of the mountain chain, and how the snow covers the vegetation in the middle of the season to finally melt and disappear by the end of the season. Fig. 2 depicts the cloud ratio for each of the 44 images. Most of the images are partially cloudy, and the pixels covered by clouds are considered as missing data. Since it is unlikely that the missing data are located in the same pixel location on consecutive acquisitions, we have interpolated the missing values using the pixel values of time adjacent images.

B. Experimental methodology

On one hand, we compared the application of both compression-based CP decomposition algorithms, CCG and ProCo ALS, to the state-of-the-art ANLS CP decomposition algorithm and to the conventional full constrained least-squares unmixing (FCLSU) independently applied on each time acquisition. In order to do that, we arranged the dataset in a tensor of $4800 \times 7 \times 44$ dimensions, corresponding to the spatial, spectral and time ways, respectively. The tensor size is convenient since it reflects the usual unbalance on the tensor dimensions, where spatial dimension is much larger than the dimensionality of the other tensor ways, while still allowing the computation of the ANLS algorithm for sake of comparison.

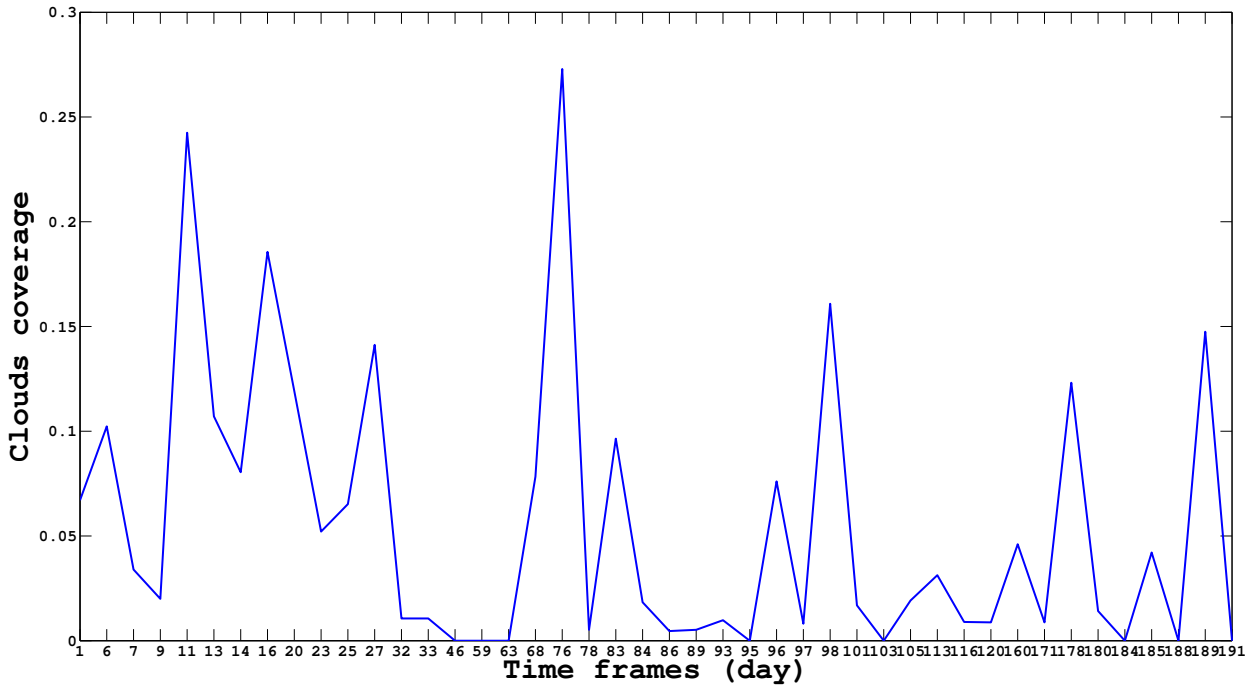

Fig. 2. Cloud coverage of the 44 time acquisitions indicated by the ratio of cloud pixels to the total number of pixels (0.00 indicates no clouds, 1.00 indicates fully covered by clouds).

We run 50 Monte Carlo runs for each of the algorithms for a set of different rank values in the range $R \in [5, 15]$. For the compression-based CP algorithms, the compressed tensor, $\boldsymbol{\mathcal{X}}_c$, has dimensions $175 \times 7 \times 25$. The comparison was done in terms of average normalized root mean squared error ($\widehat{\text{nRMSE}}$), between the original tensor, $\boldsymbol{\mathcal{X}}$, and the tensor reconstructed from the CP factors, $\hat{\boldsymbol{\mathcal{X}}}$

$$\widehat{\text{nRMSE}}\left(\boldsymbol{\mathcal{X}}, \hat{\boldsymbol{\mathcal{X}}}\right) = \sqrt{\frac{1}{NDT}\sum_{i=1}^{N}\sum_{j=1}^{D}\sum_{k=1}^{T}\left(\frac{\mathcal{X}_{ijk} - \hat{\mathcal{X}}_{ijk}}{\|\boldsymbol{\mathcal{X}}\|_F}\right)^2}.$$

On the other hand, we assessed the physical interpretability of the estimated CP factors. We compared the estimated spectral factors, $\hat{\mathbf{B}}$, to the on-field spectral measurements of eight materials (see Fig. 3), here on termed as endmembers according to the unmixing literature: *medium snow*, *glacier snow*, *old coarse*, *ice*, *debris*, *rocks*, *rain forest* and *pasture*. We made use of the spectral angular distance, d_{SAD}, to compare the pair-wise angular distances between the spectral factors and the endmembers:

$$d_{\text{SAD}}\left(\hat{\mathbf{b}}, \mathbf{e}\right) = \arccos\left(\frac{\hat{\mathbf{b}}^T\mathbf{e}}{\|\hat{\mathbf{b}}\|\|\mathbf{e}\|}\right), \tag{16}$$

where $\hat{\mathbf{b}} \in \mathbb{R}^D$ denotes a spectral CP factor and $\mathbf{e} \in \mathbb{R}^D$ denotes an endmember. In order to assess the interpretability of the spatial factors, we calculated the linear Pearson correlation of the estimated spatial factors, $\hat{\mathbf{A}}$, to the abundances estimated by a conventional FCLSU, individually applied to each of the time images, using the previously mentioned eight endmembers. Finally, we give some interpretation of the time factors, $\mathbf{C}$, in terms of the snow

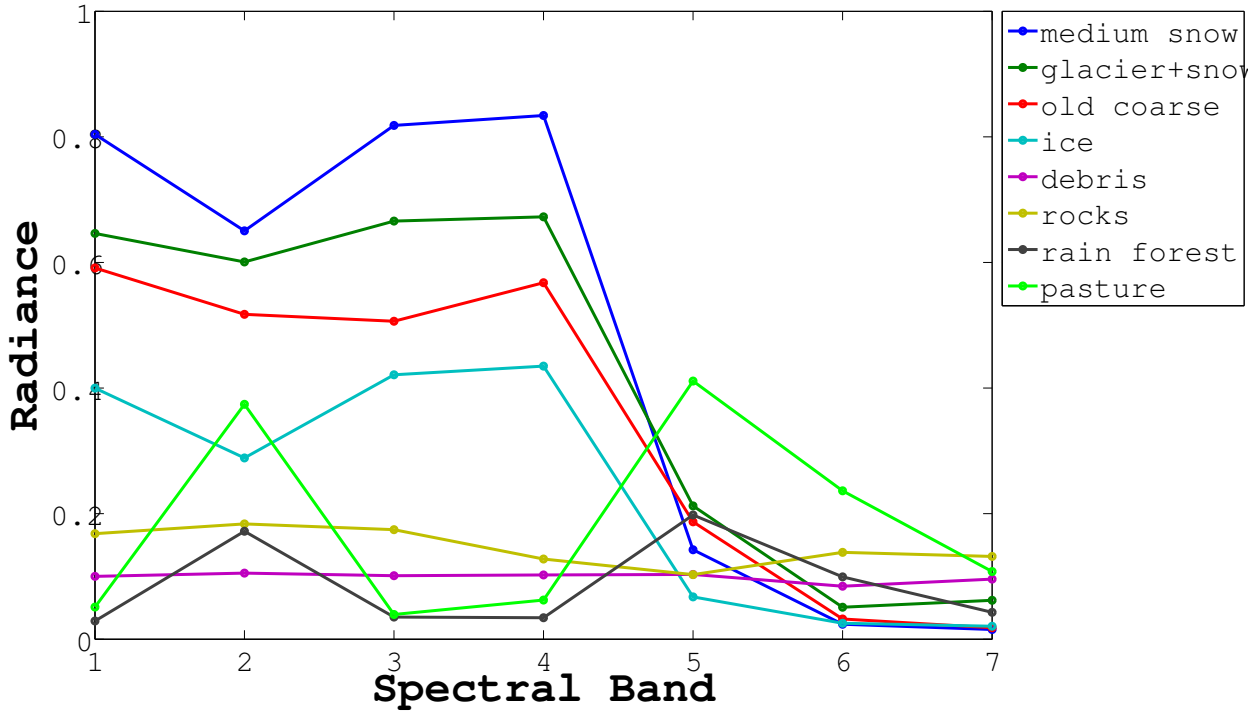

Fig. 3. On-field spectral measurements (endmembers).

season evolution.

C. Results

First, we give some overall results taking into account the performance of the competing nonnegative CP algorithms for all the evaluated rank values. The obtained results suggest that $R = 8$ is an appropriate value for this data tensor rank. Thus, we continue showing some detailed results for the best runs among the experiments with rank $R = 8$, that is the runs with minimum average normalized RMSE for each CP decomposition algorithm.

1) Overall results: Fig. 4 shows a boxplot of the average normalized RMSE of the 50 Monte Carlo runs for the different CP decomposition algorithms and rank values. The flat black line depicts the average normalized RMSE obtained by the conventional FCLSU spectral unmixing using the eight library endmembers. Overall, the compression-based algorithms achieve a performance similar to the state-of-the-art ANLS. This supports the use of the CCG and ProCoALS algorithms to perform a CP decomposition of big hyperspectral data since the computational time employed by these two algorithms is several orders of magnitude smaller than the ANLS. The ProCoALS algorithm shows less variability in the reconstruction error than CCG for small rank values. Results obtained for the rank value $R = 8$ suggests that this is a proper rank value for the CP decomposition. The CCG and ProCoALS present small error variability for rank values $R \geq 8$ compared to the ANLS algorithm, which seems to be more

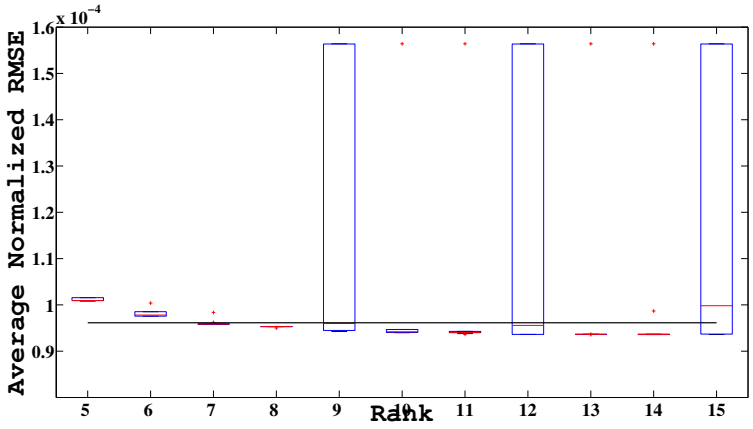

(a)

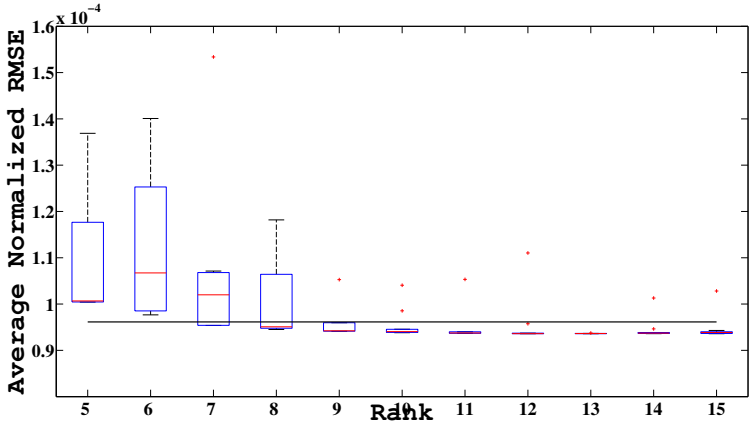

(b)

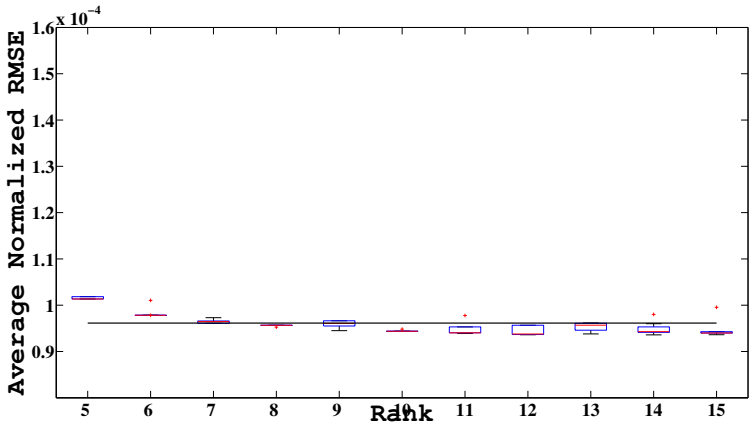

(c)

Fig. 4. Average Normalized RMSE obtained by the three competing CP decomposition algorithms: (a) ANLS, (b) CCG and (c) ProcoALS. The black line depicts the error obtained by the conventional FCLSU.

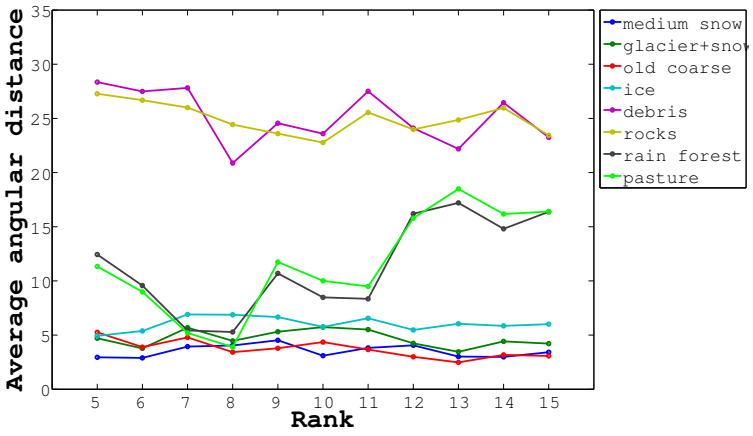

(a)

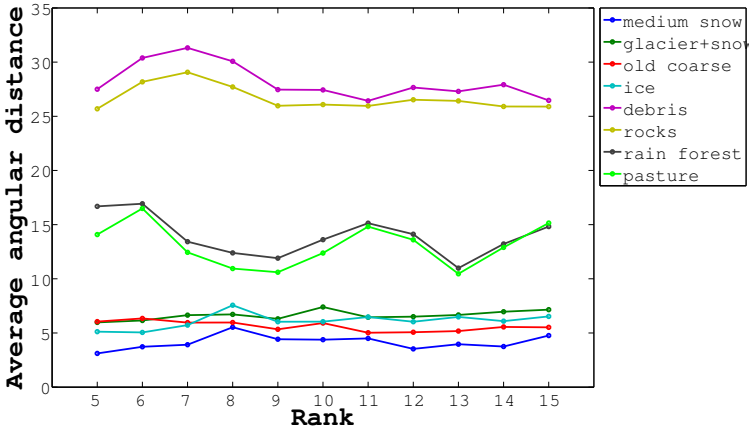

(b)

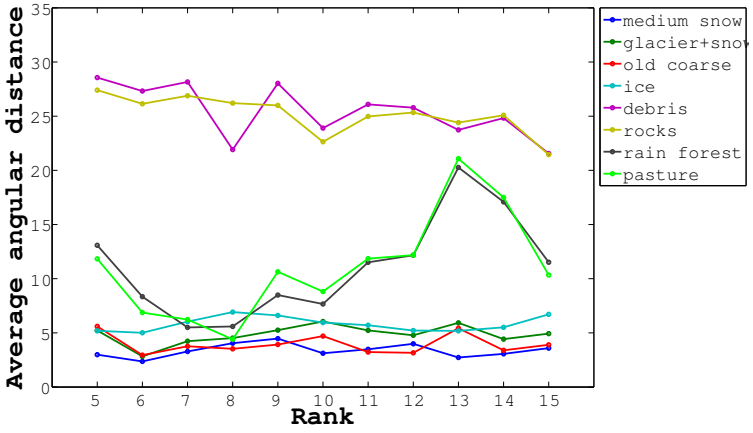

(c)

Fig. 5. Average angular distance between the eight library endmembers and the spectral factors obtained by the three competing CP decomposition algorithms: (a) ANLS, (b) CCG and (c) ProcoALS.

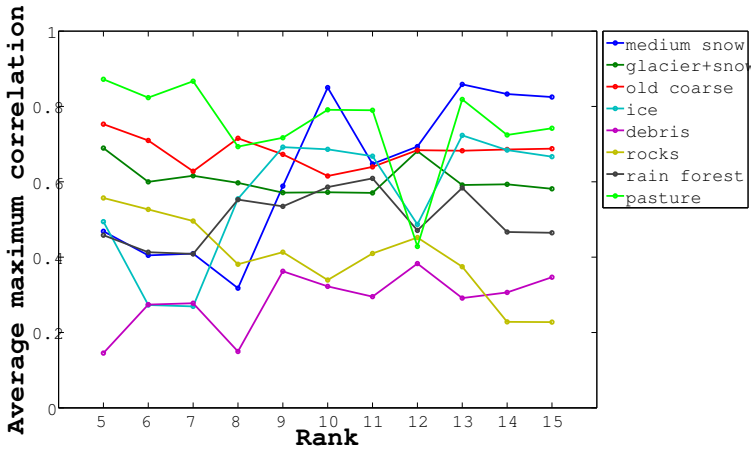

(a)

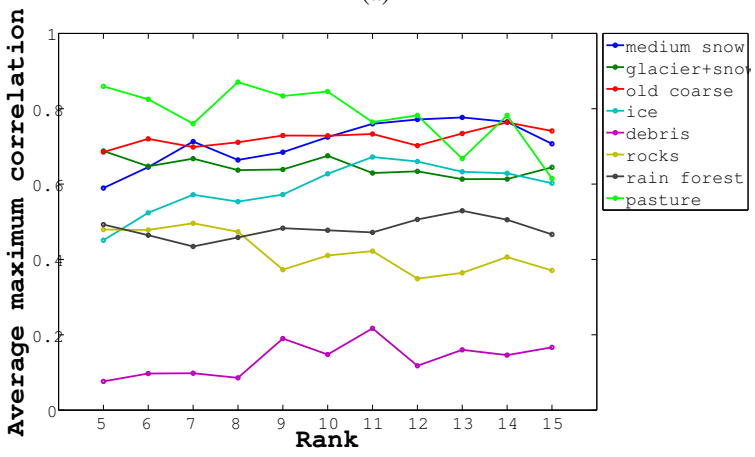

(b)

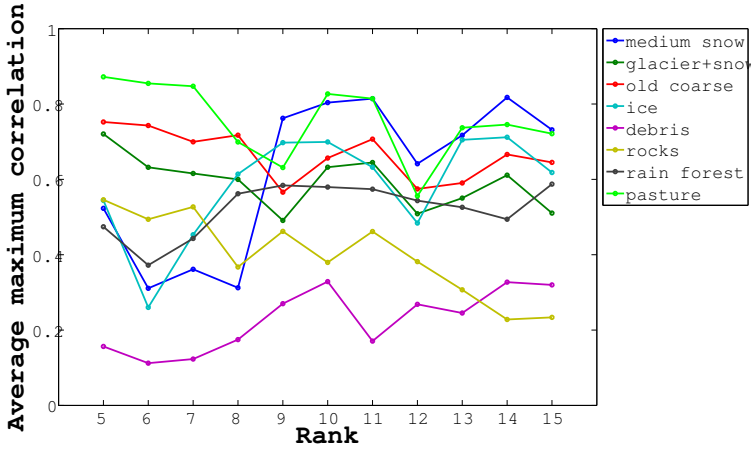

(c)

Fig. 6. Average Maximum Pearson correlation between the abundances estimated by FCLSU corresponding to the eight actual endmembers and the spatial factors obtained by the three competing CP decomposition algorithms: (a) ANLS, (b) CCG and (c) ProcoALS.

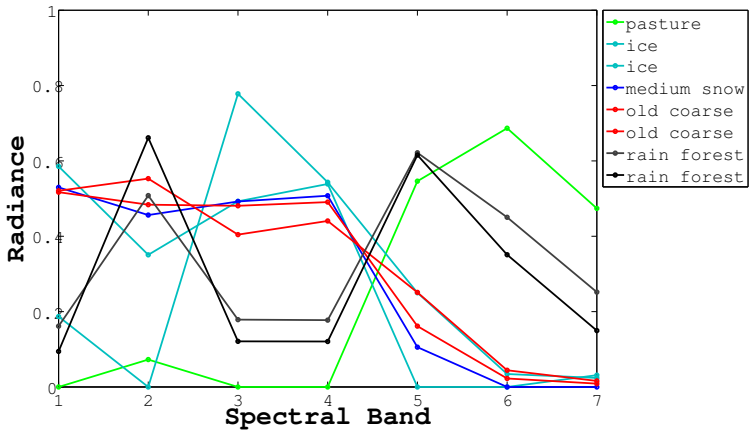

(a)

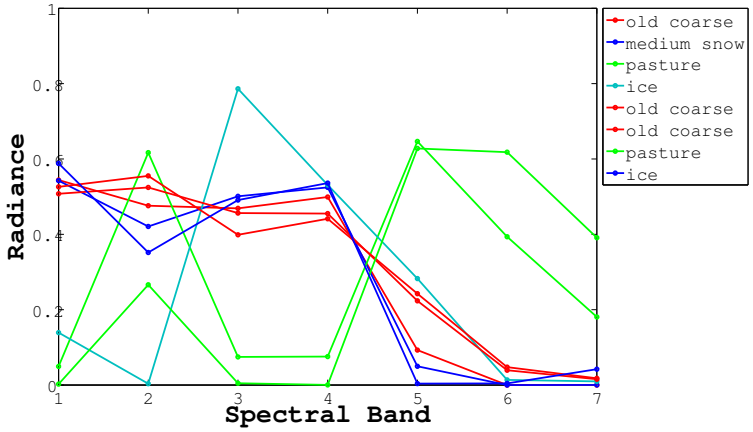

(b)

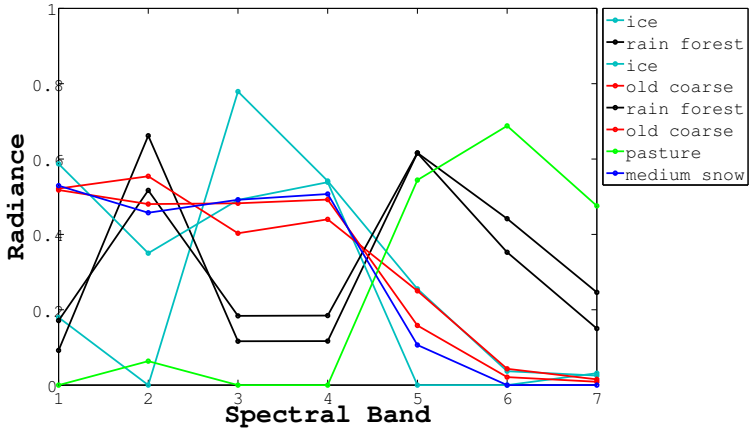

(c)

Fig. 7. Spectral factors obtained by the three competing CP decomposition algorithms: (a) ANLS, (b) CCG and (c) ProcoALS. The colours of the spectral factors correspond to their matching library endmembers.

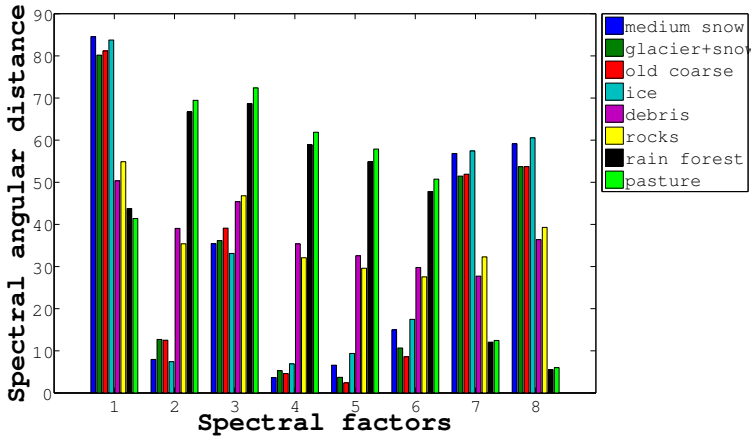

(a)

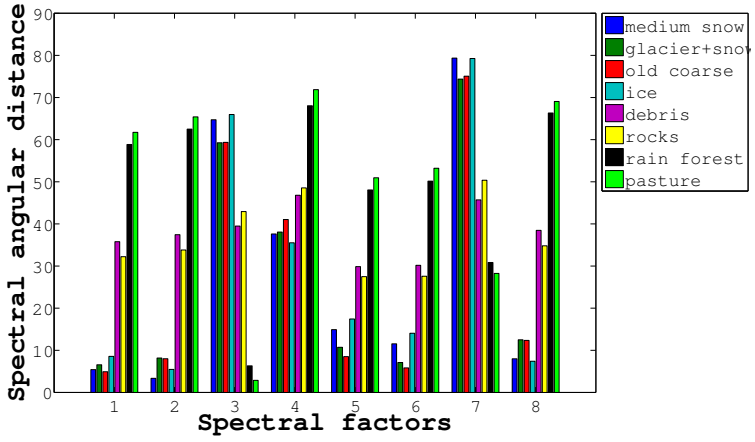

(b)

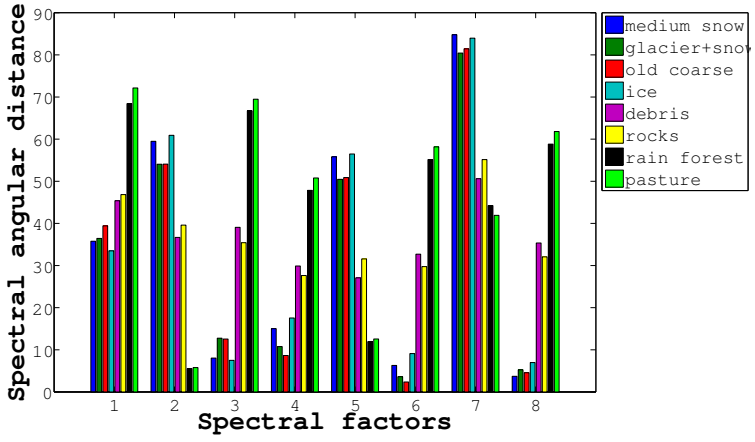

(c)

Fig. 8. Spectral angular distances between the library endmembers and the spectral factors obtained by the three competing CP decomposition algorithms: (a) ANLS, (b) CCG and (c) ProcoALS.

sensitive to an over-estimation of the tensor rank. Compared to the error obtained by the FCLSU approach, the compressed CP decomposition algorithms achieve similar or slightly better results, whilst the decomposition is more compact, i.e. the FCLSU returns 44 abundance maps for each endmember while the CP decomposition outputs $R < 8 * 44$ abundance maps and time factors.

Fig. 5 shows the average angular distance between the eight library endmembers and the spectral factors obtained by the 50 Monte Carlo runs of each of the CP decomposition algorithms. Since we want to know if the spectral factors resemble any of the library endmembers, for each run, we select the minimum angular distance from any of the estimated spectral factors to each of the eight library endmembers, and then we compute the mean among the 50 runs. All the three algorithms present the same trends. The four endmembers related to snow/ice (*medium snow*, *glacier snow*, *old coarse*, *ice*) have very small average angular distances for all rank values, meaning that these materials have been detected by the CP decomposition. The *rocks* and *debris* endmembers have high angular values meaning that the CP decompositions do not estimate any spectral factor that resembles these two materials. The *vegetation* and *pasture* are specially present for rank values close to $R = 8$, which is an additional evidence that this is a proper rank value for the data tensor. These results can be explained by the high presence of snow and ice throughout all the time series, while it is difficult to visually assess the presence of rocks and debris. Also, the almost flat spectra of these two materials could make it hard for the CP decomposition to select one of them as a spectral factor, since this information could be incorporated to the multilinear decomposition as scaling factors.

In Fig. 6 we show the average maximum Pearson correlation between the spatial factors estimated by the three CP decomposition algorithms and the spatial abundances obtained by the conventional FCLSU approach. Using the FCLSU, we obtained a set of 8 abundance maps for each of the 44 time acquisitions. We computed the Pearson correlation between the abundance maps and all the spatial factors, and for each run and library endmember, we selected the maximum Pearson correlation value. Then, we computed the mean among the 50 runs for each algorithm and rank value. Again, we obtained high correlation values for the four snow/ice materials, middle correlation values for the *pasture*/*rain forest*, and small correlations for the *debris*/*rocks*. Despite the fact that some of the materials were not detected by the CP decomposition, the presence of high correlated spatial factors indicates that they are physically meaningful and that the spatial factors could be interpretable in terms of abundances.

2) Results for $R = 8$: next, we give details about the CP factors obtained for the best run of each algorithm, in terms of average normalized RMSE, with $R = 8$. Fig. 7 shows the spectral factors obtained by the three CP algorithms. The colors indicate the library endmembers that are the most similar in angular distance to each of the spectral factors. Fig. 8 shows the spectral angular distances between the spectral factors and the library endmembers. It is interesting to mention that in all three algorithms, the spectral factors are very similar. The different matchings to the library endmembers are due to slight differences in angular distances, *i.e.* the differences among the four snow/ice spectra are very small. In the three algorithms there are two factors with high minimum spectral angle distances, factors 1 and 3 for the ANLS, factors 4 and 7 for the CCG, and factors 1 and 7 for the ProcoALS. These factors are being associated with *pasture* and *ice*, and from the shape of the factors (peaks in bands 3 and 6) it can be guessed that they correspond to a mixture of both materials.

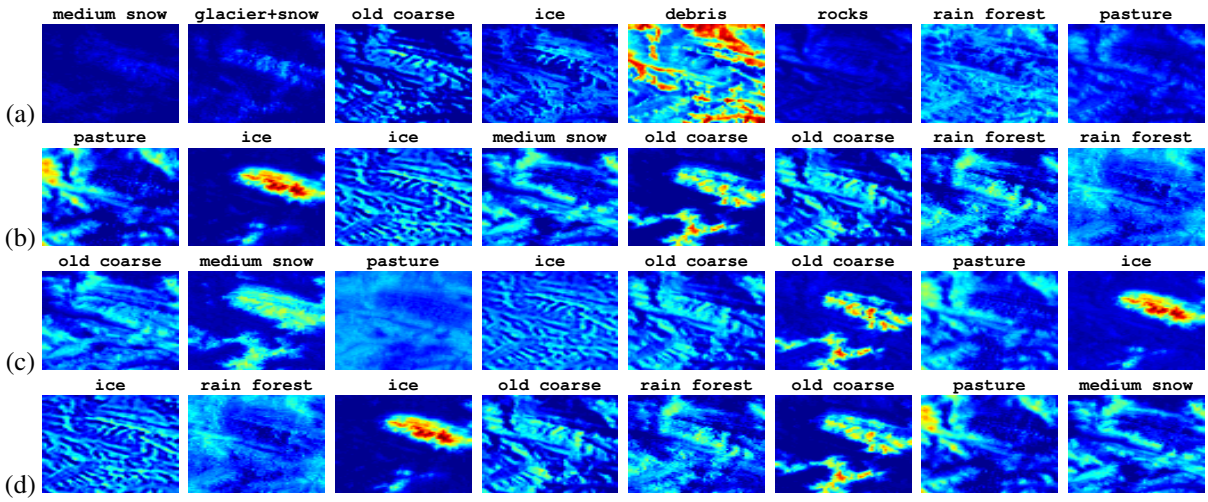

Fig. 9. (a) Spatial abundances obtained by the FCLSU averaged over the 44 time frames, (b-d) Spatial factors obtained by the three competing CP decomposition algorithms: (b) ANLS, (c) CCG and (d) ProcoALS. Each abundance map is associated to one library endmember and, for each method, scaled by the maximum value of the eight abundance maps.

Fig. 9 depicts the spatial factors as abundance maps and compare them to the average of the 44 abundance maps obtained by the conventional FCLSU approach. The spatial factors obtained by the three CP algorithms are very similar, what evidences that all three algorithms converge to the approximately same local minima given a proper tensor rank. It could be appreciated that two of the factors are related to the permanent snow/ice on the top of the mountain (factors 2 and 5 for ANLS, 6 and 8 for CCG, and 3 and 6 for ProcoALS). Also, the *rain forest* and *pasture* areas correspond to the low sides of the mountains and surrounding areas. Comparing them to those obtained by the FCLSU, it could be noted that the *debris* FCLSU abundance map has very high values compared to the remaining FCLSU abundance maps. This suggests again that its flat spectra works like a scaling factor, probably modeling spectral variability, which is a well known issue in spectral unmixing [30]. Overall, the estimated spatial factors are meaningful and the qualitative visual assessment encourages us to further investigate the use of the nonnegative CP decomposition as a multilinear "blind" spectral unmixing technique.

Finally, we provide in Fig. 10 the estimated time factors. Same as before, the colors indicate the assignment of the factors to the most similar endmembers. It is difficult to give an interpretation of the factors, but it is possible to show that they are related to the three phases of the snow season: pre-season, snow and post-season. In the pre-season and post-season the *rain forest*/*pasture* factors have a higher importance and although the ice/snow factors are present over all the season due to the permanent ice/snow areas on the top of the mountains, they have higher values during the snow and post-season phases.

V. Conclusion

Big data hyperspectral time series or multiangular acquisitions can be represented as tensors. In this paper, we have proposed the use of compression-based nonnegative CP decomposition algorithms to analyze hyperspectral

big data. We showed that the CP decomposition of hyperspectral tensors could be understood as an extension of the linear mixing model to higher-orders, that is a multidimensional blind spectral unmixing technique. We gave experimental evidence that supports the validity of the proposed approach and the physical interpretability of the tensor factors in terms of spectral signatures, fractional spatial abundances and time/angle variations. Further work will focus in the study of the proposed approach as a multilinear spectral unmixing, taking into account sparsity, spatial smoothness and other constraints usually employed in conventional spectral unmixing.

ACKNOWLEDGMENT

Authors would like to thank Prof. Isabelle Zin from the LTHE laboratory, CNRS, Prof. Marie Dumont from MeteoFrance and Dr. Mauro Dalla Mura from GIPSA-lab, Grenoble INP, for providing the experimental dataset.

REFERENCES

[1] A. F. H. Goetz, G. Vane, J. E. Solomon, and B. N. Rock, "Imaging spectrometry for earth remote sensing," *Science*, vol. 228, no. 4704, pp. 1147–1153, 1985.

[2] A. Plaza, J. A. Benediktsson, J. W. Boardman, J. Brazile, L. Bruzzone, G. Camps-Valls, J. Chanussot, M. Fauvel, P. Gamba, A. Gualtieri, M. Marconcini, J. C. Tilton, and G. Trianni, "Recent advances in techniques for hyperspectral image processing," *Remote Sensing of Environment*, vol. 113, Supplement 1, pp. 110–122, 2009.

[3] A. F. H. Goetz, "Three decades of hyperspectral remote sensing of the earth: A personal view," *Remote Sensing of Environment*, vol. 113, Supplement 1, pp. 5–16, 2009, imaging Spectroscopy Special Issue.

[4] M. E. Schaepman, S. L. Ustin, A. J. Plaza, T. H. Painter, J. Verrelst, and S. Liang, "Earth system science related imaging spectroscopy an assessment," *Remote Sensing of Environment*, vol. 113, Supplement 1, pp. 123–137, 2009, imaging Spectroscopy Special Issue.

[5] J. M. Bioucas-Dias, A. Plaza, G. Camps-Valls, P. Scheunders, N. M. Nasrabadi, and J. Chanussot, "Hyperspectral remote sensing data analysis and future challenges," *IEEE Geosci. Remote Sens. Mag.*, vol. 1, no. 2, pp. 6–36, June 2013.

[6] A. Mueller, K. Staenz, C. Ong, and U. Heiden, "International spaceborne imaging spectroscopy (isis) technical committee [technical committees]," *IEEE Geosci. Remote Sens. Mag.*, vol. 2, no. 1, pp. 18–21, March 2014.

[7] K. Frink, L. Hayden, and M. LeCompte, "Compact reconnaissance imaging spectrometer for mars (crism)," in *Geoscience and Remote Sensing Symposium (IGARSS), 2011 IEEE International*, July 2011, pp. 4078–4079.

[8] S. Bourguignon, D. Mary, and E. Slezak, "Restoration of astrophysical spectra with sparsity constraints: Models and algorithms," *IEEE J. Sel. Topics Signal Process.*, vol. 5, no. 5, pp. 1002–1013, Sept 2011.

[9] P. Comon, "Tensors : A brief introduction," *IEEE Signal Process. Mag.*, vol. 31, no. 3, pp. 44–53, May 2014.

[10] F. L. Hitchcock, "The expression of a tensor or a polyadic as a sum of products," *J. Math. Physics*, vol. 6, no. 1, pp. 165–189, 1927.

[11] H. A. L. Kiers, "Towards a standardized notation and terminology in multiway analysis," *J. Chemometrics*, pp. 105–122, 2000.

[12] J. M. Bioucas-Dias, A. Plaza, N. Dobigeon, M. Parente, D. Qian, P. Gader, and J. Chanussot, "Hyperspectral unmixing overview: Geometrical, statistical, and sparse regression-based approaches," *IEEE J. Sel. Topics Appl. Earth Observ.*, vol. 5, no. 2, pp. 354–379, Apr. 2012.

[13] D. Roberts, M. Gardner, R. Church, S. Ustin, G. Scheer, and R. Green, "Mapping chaparral in the santa monica mountains using multiple endmember spectral mixture models," *Remote Sensing of Environment*, vol. 65, no. 3, pp. 267 – 279, 1998. [Online]. Available: http://www.sciencedirect.com/science/article/pii/S0034425798000376

[14] N. Dobigeon, S. Moussaoui, M. Coulon, J.-Y. Tourneret, and A. Hero, "Joint bayesian endmember extraction and linear unmixing for hyperspectral imagery," *IEEE Trans. Signal Process.*, vol. 57, no. 11, pp. 4355–4368, Nov 2009.

[15] O. Eches, J. Benediktsson, N. Dobigeon, and J.-Y. Tourneret, "Adaptive markov random fields for joint unmixing and segmentation of hyperspectral images," *IEEE Trans. Image Process.*, vol. 22, no. 1, pp. 5–16, Jan 2013.

[16] J. E. Cohen, R. C. Farias, and P. Comon, "Fast decomposition of large nonnegative tensors," *IEEE Sig. Proc. Letters*, vol. 22, no. 7, pp. 862–866, Jul. 2015, accepted in nov. 2014.

[17] J. Cohen and U. Rothblum, "Nonnegative ranks, decompositions and factorizations of nonnegative matrices," *Lin. Alg. Appl.*, vol. 190, pp. 149–168, 1993.

[18] L.-H. Lim and P. Comon, "Nonnegative approximations of nonnegative tensors," *J. Chemometrics*, vol. 23, no. 7-8, pp. 432–441, 2009.

[19] J. B. Kruskal, "Three-way arrays: Rank and uniqueness of trilinear decompositions," *Lin. Alg. Appl.*, vol. 18, pp. 95–138, 1977.

[20] L. Chiantini, G. Ottaviani, and N. Vannieuwenhoven, "An algorithm for generic and low-rank specific identifiability of complex tensors," *SIAM J. Matrix Ana. Appl.*, vol. 35, no. 4, pp. 1265–1287, 2014.

[21] Y. Qi, P. Comon, and L.-H. Lim, "Uniqueness of nonnegative tensor approximations," Oct. 2014, arxiv:1410.8129.

[22] P. Paatero, "A weighted non-negative least squares algorithm for three-way parafacfactor analysis," *Chemometrics and Intelligent Laboratory Systems*, vol. 38, no. 2, pp. 223–242, 1997.

[23] A. Cichocki, R. Zdunek, A. H. Phan, and S.-I. Amari, *Nonnegative matrix and tensor factorizations: applications to exploratory multi-way data analysis and blind source separation*. John Wiley & Sons, 2009.

[24] R. Bro, "Multi-way analysis in the food industry: models, algorithms, and applications," Ph.D. dissertation, University of Amsterdam, The Netherlands, 1998.

[25] L. De Lathauwer, B. De Moor, and J. Vandewalle, "A multilinear singular value decomposition," *SIAM J. Matrix Ana. and Appl.*, vol. 21, no. 4, pp. 1253–1278, 2000.

[26] N. Sidiropoulos, E. Papalexakis, and C. Faloutsos, "Parallel randomly compressed cubes: A scalable distributed architecture for big tensor decomposition," *IEEE Signal Process. Mag.*, vol. 31, no. 5, pp. 57–70, 2014.

[27] G. Zhou, A. Cichocki, and S. Xie, "Decomposition of big tensors with low multilinear rank," *arXiv preprint arXiv:1412.1885*, 2014.

[28] A. P. Liavas and N. D. Sidiropoulos, "Parallel algorithms for constrained tensor factorization via the alternating direction method of multipliers," *arXiv preprint arXiv:1409.2383*, 2014.

[29] S. J. Wright and J. Nocedal, *Numerical optimization*. Springer New York, 1999, vol. 2.

[30] A. Zare and K. Ho, "Endmember variability in hyperspectral analysis: Addressing spectral variability during spectral unmixing," *IEEE Signal Process. Mag.*, vol. 31, no. 1, pp. 95–104, Jan 2014.

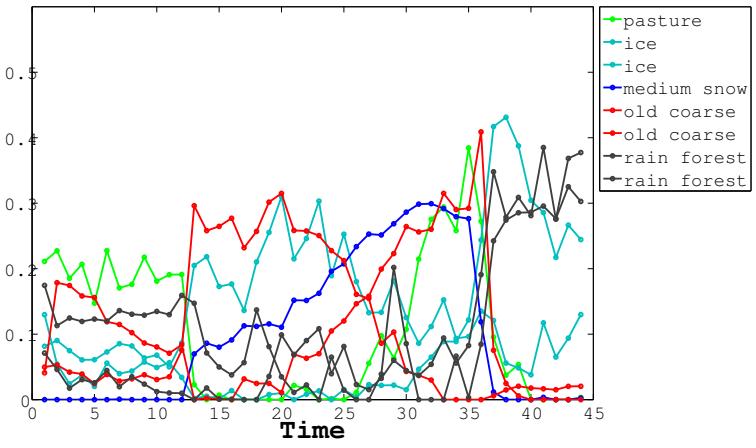

(a)

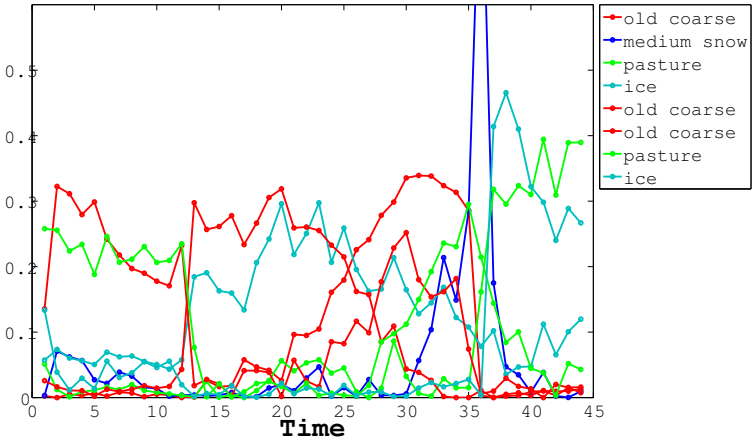

(b)

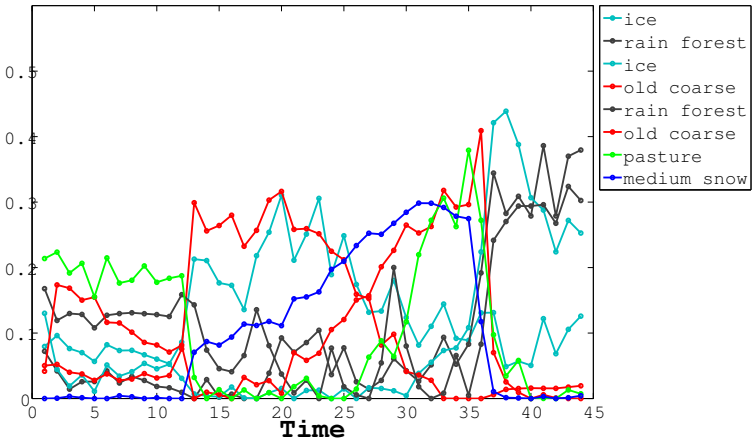

(c)

Fig. 10. Time factors obtained by the three competing CP decomposition algorithms: (a) ANLS, (b) CCG and (c) ProcoALS. The colours of the time factors correspond to their matching library endmembers.